Technical Design Report

Johns Hopkins University
Collegiate Wind Competition 2022

Submitted April 24, 2022

Aerodynamics Team
Hojun Lee (Lead)
Kathy Cao, Woojin Choi, Isaac Lee, Justin Lee

Structures Team
Kathy Cao (Lead)
Julia Choe, Brennan Hughes, William Rong

Electronics and Controls Team
Eleni Daskopoulou (Lead)
Daniel Okereke (Lead)
Shivanie Ally, Yared Kokeb, Jonathan Young

Generator Team
Zach Galvarro (Lead)
Isaac Lee (Lead)
David Corrente

With assistance from Dennice Gayme and Rui Ni, Faculty Advisors

Table of Contents:

1.0 Executive Summary

For our entry to the Collegiate Wind Competition, the JHU team aimed to maximize the efficiency of an off-shore wind turbine that complies with the space and structural requirements of the competition.

This year we were challenged to design an offshore fixed bottom foundation. To meet this goal we chose to design a modified monopile. Using campus resources, we tested our design for horizontal displacement and load to failure. For the structural design, we also redesigned our nacelle to accommodate for the single-rotor horizontal axis design we chose to pursue this year.

Our blades are derived from NACA 6409 airfoil which is well suited for our low low-Reynolds number application [1]. We optimized blade geometry for given flow conditions. We then incorporated dimples on the blade surface to maximize power, after comparing their power and RPM performances with those from blades without dimples. The final blade geometry was 3D printed with ABS and smoothed with acetone vapor bath to even out surface finish.

The peak efficiency was 16.3% and although it is lower than last year's peak efficiency, we were able to discover the potential of having dimples on the blade surface. In the future, we are interested in varying the size and location of the dimples and identifying the optimal combination that results in maximum efficiency.

The generator system we designed is composed of a brushless DC motor whose three-phase power output is then rectified and smoothed to approximate a DC output. We started with theoretical modeling of motors, and then selected two motors that suggested they would be able to provide positive power outputs. These motors were then subject to testing that emulated the wind tunnel conditions anticipated and from that data we selected our final motor, the BL23E22.

Our turbine is primarily operated by a microcontroller (MCU) controlling the load resistance and the blade pitch to optimize power output and brake the turbine during the safety task. This pitching system is complemented by a solenoid-based mechanical brake to ensure the cessation of turbine operation and increase robustness. An additional microcontroller is used to synchronize shutdown processes and ensure the restart of the turbine, through inter-MCU optically isolated digital communication. This dual-MCU approach reduces the complexity associated with the hardware-based transistor approach from last year's implementation.

2.0 Technical Design

2.1 Design Objective

For the 2022 Collegiate Wind competition, our team was asked to research, design, and build an offshore wind turbine. Due to the added challenge of mounting the turbine in water, our efforts were focused on designing a foundation structure that would keep the turbine stable during operation, without compromising power efficiency.

2.2 Rotor and Blades

Our single rotor system was designed to effectively capture kinetic energy of the wind. The blades' shape and geometry were selected and optimized for the provided flow condition. This year, we were interested in incorporating dimples on the blades' surface to maximize aerodynamic performance of our turbine and this concept was explored throughout the design process. Testing our turbine with an active pitch control system, we were able to obtain characteristics of our turbine in a wide range of wind speeds.

2.2.1 Base Aerodynamic Design and Analysis

The blade's airfoil was selected based on its aerodynamic performance at low Reynolds numbers (Re < 100,000). A literature survey suggested NACA 6409 shows a better power curve at low wind speed ranges than at higher speeds [1]. Similarly, the S1210 airfoil, which we used in CWC 2021, is an airfoil originally designed for a small length scale and has been adopted in small-scale wind turbine research [2][3]. Hence, both NACA 6409 and S1210 were considered. First, the maximum ratio of lift coefficient to drag coefficient (C_l/C_d) for each blade and the corresponding angles of attack (AOA) were obtained

from QBlade. For these simulations, the input *Re* was set to be ~21000, which was based on the average wind speed required and last year's team's average chord length. The result showed that NACA 6409 has a higher maximum C_l/C_d at this *Re* and this was verified by conducting a 2D CFD simulation in ANSYS CFX for both airfoils which led us to select NACA 6409 as the base airfoil. The shape of NACA 6409 is shown in figure 1.

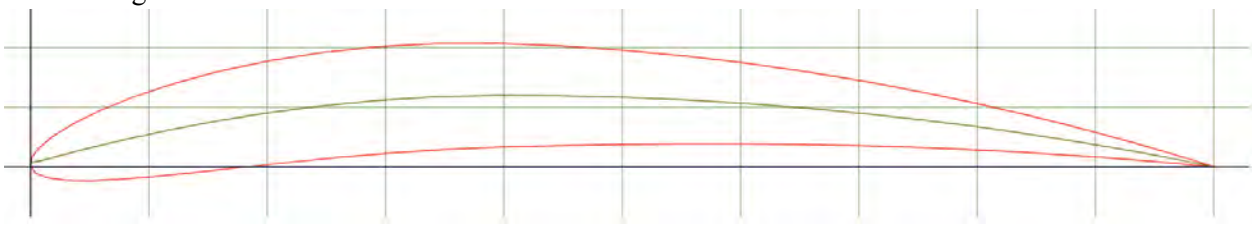

Figure 1. The NACA 6409 Airfoil [4]

After selecting airfoil, we constructed the blade geometry in QBlade. The initial blade length, the chord length variation, and the tip speed ratio (TSR) of 4.5 from last year's team's blade design were used as the initial inputs for the optimization. The rotor diameter was set to be 44 cm with our active pitch hub radius 3.5 cm, allowing our blade length of 18.5 cm. We then used the Schmitz optimization process [5], considering its additional wake effect factor [6], to optimize the angle of twist and chord length array for 11 sections along the blade for the AOA correlated with the maximum C_l/C_d. The optimized blade geometry was exported as an STL file for further additions in Solidworks.

2.2.2 Dimpled Blades Design and Analysis

As dimples are known to delay flow separation and increase the C_l/C_d for golf balls [7], we explored a dimpled blade design. Since several studies suggested increased turbine efficiency after incorporating dimples [8][9][10], we were curious to see if the same effect could be observed for our small-scale wind turbine. Hence, 2D turbulence simulations were conducted through ANSYS CFX for NACA 6409 with varying numbers of dimples and AOA at a wind speed of 6.5 m/s. The dimple diameters were set as 5% of the average blade chord length of 0.05 m, and the Shear Stress Transport turbulence solver was used with inputs from literature [8][9]. The mesh used for a simulation is shown in Figure 2.

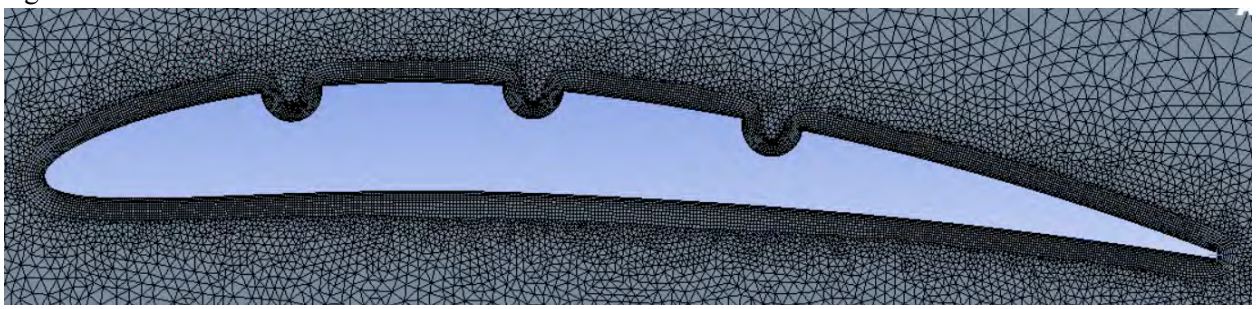

Figure 2. Mesh around NACA 6409 airfoil with three dimples for the 2D turbulence simulation

Results, as shown in figure 3, demonstrate that the no-dimple design at 4º AOA yields the highest C_l/C_d among the considered designs, including those with dimples. However, the C_l/C_d increases relative to the number of dimples from one to three, which suggests a larger number of dimples could lead to higher values of C_l/C_d. The limitations of 2D simulations may have underestimated the effects of dimples. Moreover, literature suggests that decreasing the dimple sizes may enhance the aerodynamic performance which led us to implement smaller dimples in our design [9].

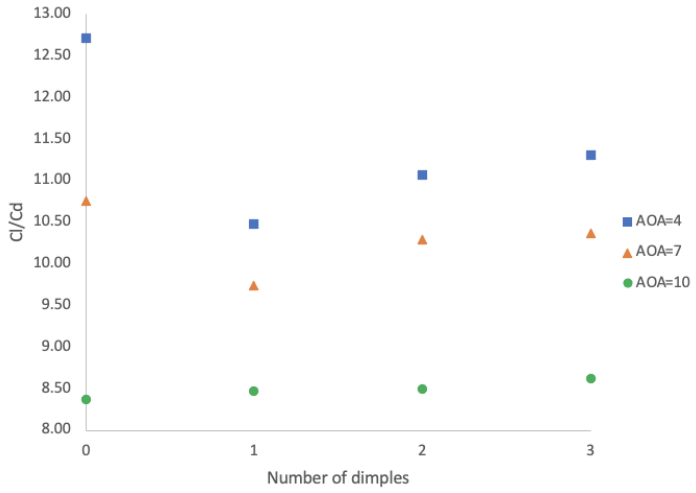

Figure 3. Number of dimples vs. C_l/C_d at varying angles of attack (AOA)

For the actual blade design, six dimples with diameter of 2.5% chord length were equally spaced along the chord of each section of the blade. Solidworks was used to incorporate dimples on blade geometry from Qblade optimization, and placing of the dimples followed that in [ref8]. Dimples were added to eight sections of the blade, resulting in 48 dimples in total per blade. In order to compare the performance of the dimpled blades to the no-dimpled blades, both types of blades were 3D printed for testing.

2.2.4 Rotor Fabrication and Assembly

For our rotor hub, we used a modified hub from the JCZK 300C RC helicopter from last year's team shown in figure 4 to achieve active pitch control. A linear bearing is mounted along the shaft to minimize vibration during pitch control and make sure that all three blades pitch together. In order to mount the blades to the rotor hub, appropriate mounting geometry was added to the root of the blade in Solidworks. The pitch system is attached to Actuonix L12 linear actuator with 3D printed coupler to obtain precise pitch control.

Figure 4. JCZK 300c Rotor Hub

The blades and custom mounting parts were 3D printed from ABS with solid infill. Here, ABS was chosen for its relatively high strength. Initial blade prototypes were printed on Qidi X-Plus 3D printer and were post-processed in acetone vapor bath to ensure smooth surface. Parts requiring higher degree of accuracy printed on University-owned UPrint SE Plus printer and post-processed in sodium hydroxide solution. The final blade prototypes are shown in Figure 5.

Figure 5. Final blade prototypes: with dimples (left three) and without dimples (right three)

2.2.4 Aerodynamic Testing Methods and Results

To test power-generating performance of our rotor and blades, we conducted a series of testing in our school's 1-m wind tunnel. For each wind speed we measured the load voltage, load current, rotor RPM, while controlling the linear actuator position (thus controlling the blade pitch) and variable load. First, RPM and power outputs of blades with and without dimples were measured for comparison. Figure 6 shows that within the wind speed range of 6-9 m/s, dimpled blades output higher RPM and power compared to blades without dimples. Thus, we decided to do further testing with dimpled blades. Note that this data is from preliminary testing done early this year before finalizing design decisions for other parts of the rotor such as the pitch control method. This led to lower power and RPM compared to our final results in figure 7.

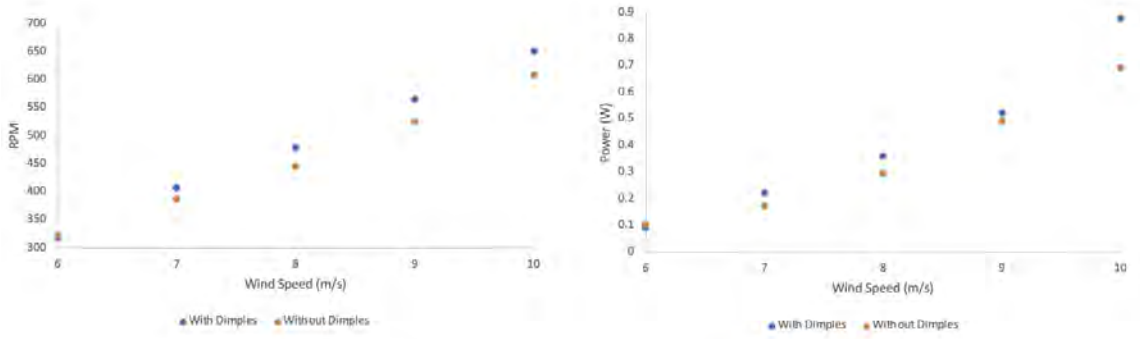

Figure 6. RPM and power output from dimpled and non-dimpled blades at different wind speeds

For further testing of the dimpled blades, we varied wind speed from 5 to 11 m/s in 1m/s increments. Moreover, using our active pitch control system, we varied our blade pitch at each wind speed to control TSR. Variable load was also used to control TSR, which will be explained in more detail in a later section of this report. From the testing, we obtained power coefficient (Cp) and TSR for each blade pitch and the resulting Cp vs. TSR plot at different pitch angles are shown in Figure 7. This shows our peak performance was obtained at TSR of 2.8. The maximum Cp was 16.3% which was obtained at pitch angle of -7 degrees when TSR = 3.

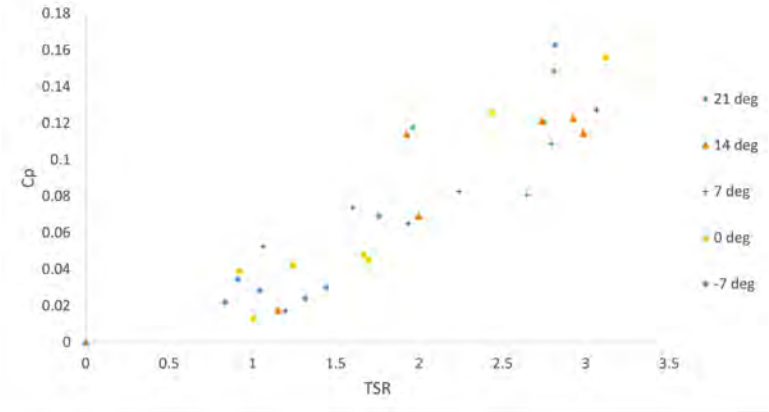

Figure 7. Cp vs. TSR at each blade pitch angle

2.3 Generator and Powertrain System

2.3.1 Initial performance modeling

The purpose of the generator and powertrain system is to maximize the weighted power performance of our turbine at wind speeds between 5 and 11 m/s. Considering the single-rotor design of this year's turbine, we chose a direct transmission system that minimizes power losses from more interfaces.

2.3.2 Numerical simulation

We calculated the maximum rpm of the generator using the known wind speeds as well as blade TSR and dimensions, and the maximum torque on the generator was derived from the mechanical power equation for a rotating shaft. Weighted scores for each motor were determined from maximum theoretical power calculations as well as the scoring rubric specified by the Collegiate Wind Competition (Figure 8).

Motor Model BL23E48-02

Speed/voltage constant (v/krpm)	9.6	(v / No load speed)
Torque constant (Nm/Amp)	0.096	
Winding resistance (ohms)	0.44	
Cogging torque (Nm)	N/A	

Wind Speed Bins (m/s)	RPM	Kinetic Power	Torque Input (Nm)	Voltage (V)	Current (Amp)	P Loss to Heat (W)	P out (W)	Req In P (W)	Net P Out	Wind Speed Rated Power Score	Rated Score
5	955	11.6	0.0	9.2	0.31	0.04	2.9	2.9	2.8	0.7	1.98
6	1146	20.1	0.0	11.0	0.42	0.08	4.6	4.7	4.5	0.8	3.61
7	1337	31.9	0.1	12.8	0.52	0.12	6.7	6.8	6.6	0.8	5.25
8	1528	47.7	0.1	14.7	0.62	0.17	9.2	9.3	9.0	0.7	6.30
9	1719	67.9	0.1	16.5	0.73	0.23	12.0	12.3	11.8	0.4	4.72
10	1910	93.1	0.1	18.3	0.83	0.31	15.3	15.6	15.0	0.3	4.49
11	2101	124.0	0.1	20.2	0.95	0.40	19.1	19.5	18.7	0.1	1.87
										Weighted Score	**28.21**

Motor Model UAV MN6007

Speed/voltage constant (V/krpm)	160	
Torque constant (1/speed constant)	0.625	
Winding resistance (ohms)	2.4	
Cogging torque (Nm)	N/A	

Wind Speed Bins (m/s)	RPM	Kinetic Power	Torque Input (Nm)	Voltage (V)	Current (Amp)	P Loss to Heat (W)	P out (W)	Req In P (W)	Net P Out	Wind Speed Rated Power Score	Rated Score
5	955		0.0	1.5	0.05	0.01	0.1	0.1	0.1	0.7	0.05
6	1146		0.0	1.8	0.06	0.01	0.1	0.1	0.1	0.8	0.09
7	1337		0.1	2.1	0.08	0.02	0.2	0.2	0.2	0.8	0.12
8	1528		0.1	2.4	0.10	0.02	0.2	0.3	0.2	0.7	0.15
9	1719		0.1	2.8	0.11	0.03	0.3	0.3	0.3	0.4	0.11
10	1910		0.1	3.1	0.13	0.04	0.4	0.4	0.4	0.3	0.11
11	2101		0.1	3.4	0.15	0.05	0.5	0.5	0.4	0.1	0.04
										Weighted Score	**0.67**

Figure 8. Calculation Comparisons Table

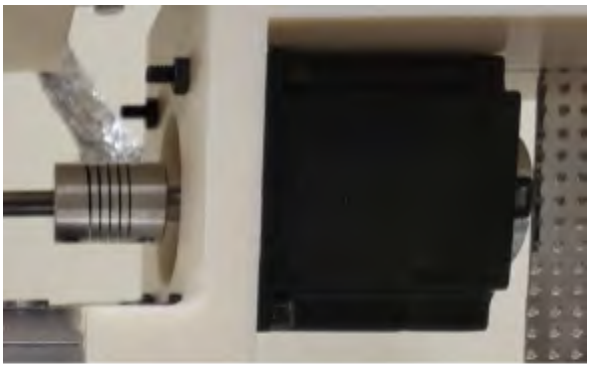

Figure 9. BL23E22-02 motor

Figure 10. MN6007 motor

However, the accuracy of the comparison calculations were largely dependent on the access to motor specifications, especially when considering sources of power loss. We reached out to various motor suppliers for specifications, like cogging torque, that were

outside of the scope of standard motor specification sheets. However, much information could not be gathered for most of the considered motors. Thus, the calculations for weighted power were approximated solely to be used as a basis for comparing motors and a rough estimate of possible power production. Through this preliminary process, we narrowed down two main motors to be validated through testing—the Lin Engineering BL23E22-02 (Figure 9) for its higher power production performance and the TMotor UAV MN6007 KV160 (Figure 10) for its potential as a drone motor, which is much lighter and has a more efficient cooling structure.

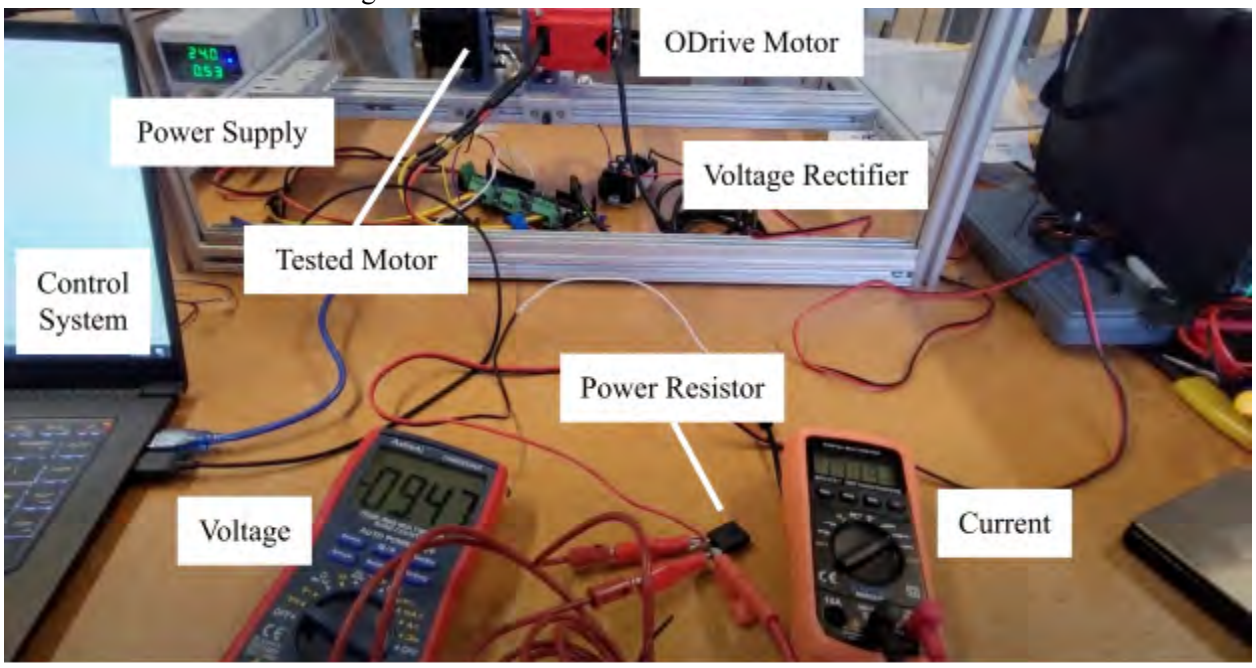

Figure 11. Dynamometer Testing Setup

2.3.3 Simulation validation

We purchased the two motors from the calculation comparisons and put them through testing on a dynamometer (Figure 11). We simulated generators being driven by a rotor using the ODrive motor with a torque-control feature. The tested motor's power outputs were measured at incremented torques that were determined in Figure 8. In practice, the torque control abilities of the dynamometer were highly inconsistent. Thus, the theoretical rpm of the shaft at each wind speed was used instead through a rotational velocity-control feature of the ODrive system. Although some data could be collected for the lower wind speeds (Figure 12), we were unable to consistently drive the dynamometer motor at higher speeds throughout testing. Thus, further validation was defaulted to directly testing each of the motors in the wind tunnel with the wind turbine. However, the dynamometer system provided a foundation for validated comparisons to choose the optimal motor. With the limited testing we were able to do on the dynamometer and later in the wind tunnel, we found that the BL23E22-02 motor outperformed the

Motor	Wind Speed (m/s)	Dyno RPM	Voltage (V)	Current (mA)	Power (W)
BL23E22	5	955	6.48	117.2	0.76
	6	1146	7.98	144.3	1.15
MN6007	5	955	4.75	85.3	0.41
	6	1146	5.91	106.2	0.63

Figure 12:Testing data collected from dynamometer

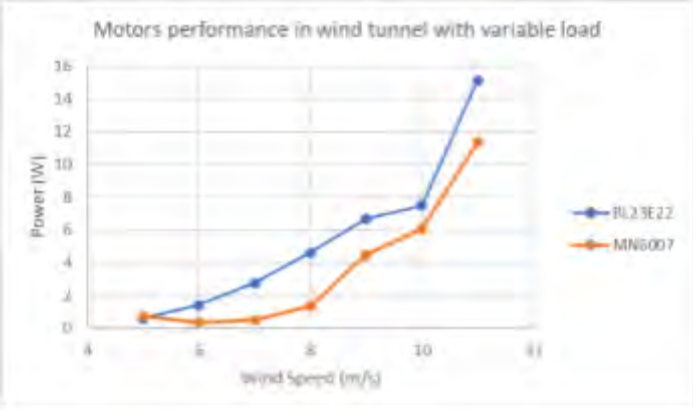

Figure 13. Motors Performance

MN6007 motor by a large margin (Figure 13).

2.3.4 Converting and stabilizing power

The chosen generator produces a 3-phase AC voltage which we convert to DC voltage using a 3-phase full wave rectifier. This maximizes the converted power and produces a relatively stable power output that can be transmitted and dissipated at the load.

During testing, we noticed that the periodicity of the rectified power produced by the generator compromised the stability of our power output. We thus decided to create a low pass filter by connecting a capacitor in parallel with the power line, to prevent oscillations from propagating to the PCC and our load. Competition rules allow for a ±10% in power which translates to a $\pm\sqrt{10}\%$ oscillation in voltage (which corresponds to Vpp = 0.45V at minimum wind speed). The oscillation frequency at minimum was calculated as $f = \frac{poles * rpm}{120} = 22Hz$ [12] . Using the formula $C = \frac{I}{2*f*Vpp}$ (with I = 0.55A for that wind speed) we calculated the minimum required capacitance to be C=0.028F [11]. This capacitor was added in parallel with the generator.

2.4 Electronics and Controls

During normal operation of the turbine, the electronics are primarily used to optimize power generation. This is accomplished with controlling the blade pitch and the load resistance for power dissipation.

2.4.1 Blade pitching

As determined through initial testing, blade pitching significantly affects the performance of the turbine. Thus, we developed and tested two approaches for pitching the blades at different wind speeds.

The first one relied on taking voltage and current measurements in real-time to calculate the generated power output. Then, through a feedback control algorithm the MCU would try to adjust the linear actuator position (which adjusted the blade pitch) to maximize the measured power. Even though that approach would have been more robust and independent of small variations in the turbine assembly and environmental conditions, we determined not to deploy it due to small variations in the power output (even when the wind speed was stable) which caused the algorithm to try and change the blade pitch thus wasting power.

The second approach, which we decided to use, relies on extensive testing to determine the optimum blade pitch value for different wind speeds. We then extrapolate the wind speed by measuring the RPMs of the rotor and using hardcoded lookup tables and adjust the blades to the optimal pitch angle. It is significant to note that determining the wind speed through RPM measurements is challenging because the rotor's rotations are affected by both blade pitch and load resistance. Thus, we decided to have a calibration phase when a wind speed change outside normal variations is detected. During that phase, we pitch the blades at a certain angle and set a known resistance value, so that we can always reliably compare the RPM to a set baseline.

2.4.2 Variable Load

As mentioned earlier, the load resistance also affects the produced power, so we designed and manufactured a variable load system by connecting power resistors in parallel that can be controlled by the MCU through transistors and high power relays (Appendix C).

We determined the optimum resistance value at the optimum blade pitch for each wind speed through testing. These values are then hardcoded in the turbine and load MCU firmware.

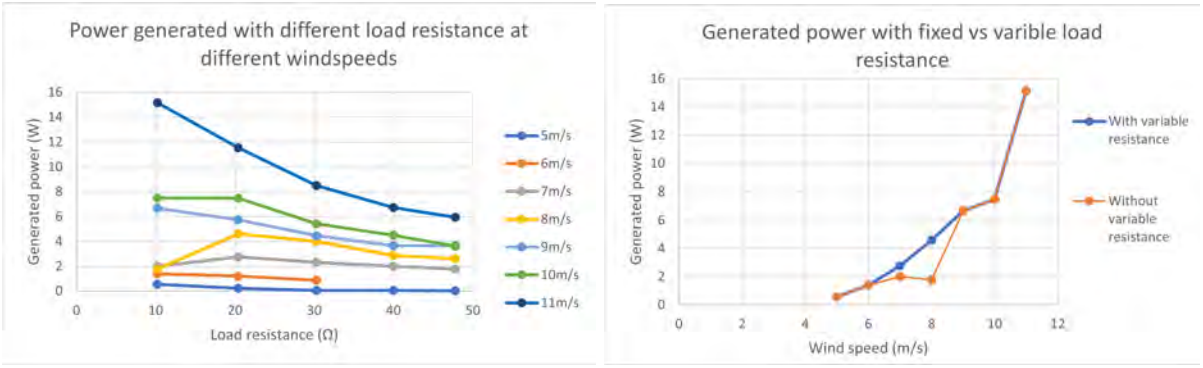

Figure 14. Effect of load resistance on measured power

2.4.3 Safety System

To accomplish the safety task, we decided to use two microcontrollers with one on the turbine side and one on the load side. The load side MCU is powered through a wall adapter and is mainly responsible for detecting a load disconnect or safety button press. When this event occurs, it sends a signal to the turbine side MCU to initiate braking. Furthermore, when the turbine stops producing power, it connects 5V power scaled down through the wall adapter to the main power line, so that the turbine side MCU can function when exiting the safety state. The turbine side MCU enters the safety state when it receives the corresponding signal from the load side MCU. It then proceeds to activate our braking mechanisms while also disconnecting the generator from the main power line (through the turbine side latching relay). All the communications between the two microcontrollers happens through digital I/O signals and pins. Optocouplers were used to optically isolate all lines crossing the PCC other than the main power line. An additional four optocouplers (not shown) are used to control the variable load from the turbine side.

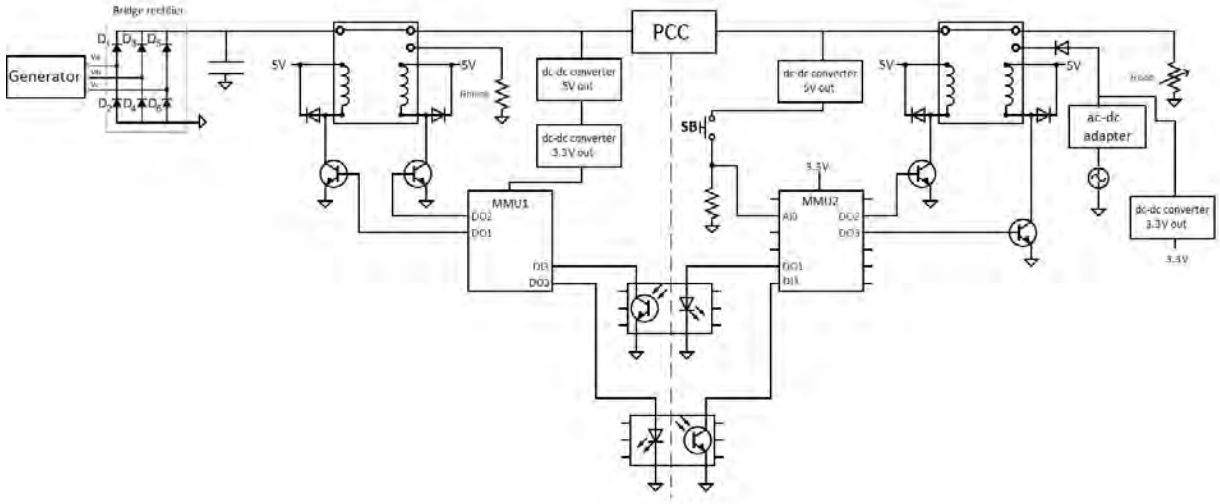

Figure 15. Complete Electronics System Circuitry

2.4.4 Braking mechanism

Braking occurs in two steps: a solenoid as a mechanical, reliable,and electronic-independent brake that is activated with loss of power and a blade pitch-based brake so that mechanical forces from sudden braking are minimized by slowing down the rotor first. During normal operation, current will flow

through the solenoid, generating a magnetic field to retract the shaft so that it does not interfere with the rotor and it can spin freely. Once a braking signal is received, the turbine MCU will pitch the blades at a feathering position (blades are parallel to air flow), causing the turbine to slow down. After 7 seconds or when power is no longer produced (whichever occurs first), the solenoid will stop getting power which will cause the magnetic field to dissipate, such that there is no force opposing the solenoid's spring. The spring will return to its neutral position, meshing the solenoid's stub with the rotor's braking disc to mechanically lock the rotor in place. In the event that the voltage generated exceeds 45V, the blades will be pitched to reduce RPM without engaging the mechanical brake to allow for continuous operation during the Durability Task.

To validate our design, we attached the disc to a BEMONOC 25GA370 12V DC motor and powered it through a power supply at different voltages to achieve different speeds. Then, we secured the solenoid at the edge of a table to represent its position on the actual turbine and powered it with another power supply. We ran the motor from 5V to 12V with a step size of 1V to achieve a range of angular velocities which were converted to RPMs. Both the rotor disc and solenoid withstood speeds as high as 848 RPM without damage or other visible stress which is sufficient when coupled with the prior speed reduction from blade pitching.

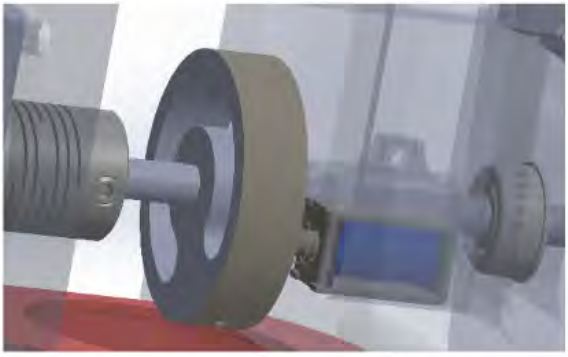

Figure 16: Solenoid and Gear of Mechanical Brake

2.4.5 Firmware development

The firmware for both the turbine side and load side MCUs was developed incrementally such that programs for each part of our system were written and tested individually. For all initial testing, we used an Arduino Uno as the main MCU due to its compatibility with many breakout boards and the convenient IDE environment and libraries. Once we had finalized the electronics and code of the subsystem, we moved to using MSP430/MSP432 MCUs which are being used in the final design due to greater power efficiency. This shift also required moving the code to Energia, a platform allowing Arduino code execution on Texas Instruments MSP series MCUs. The following figures schematically explain the main procedures and controls managed by each MCU.

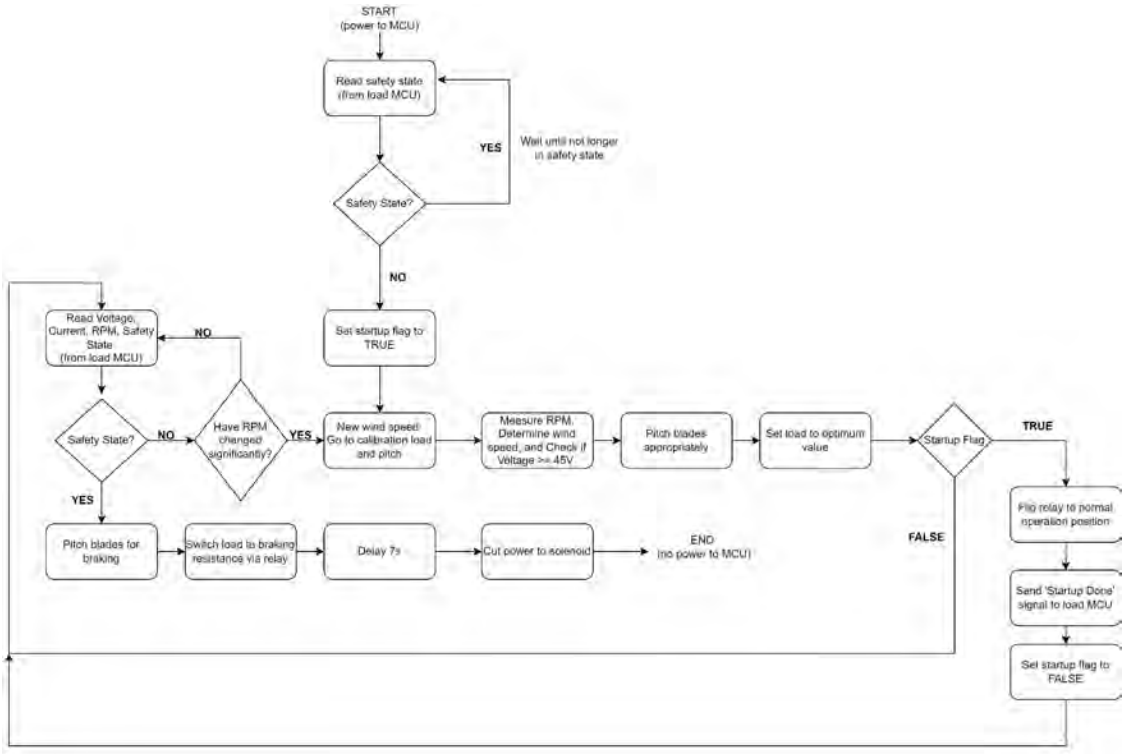

Figure 17: Finite state diagram for turbine MCU

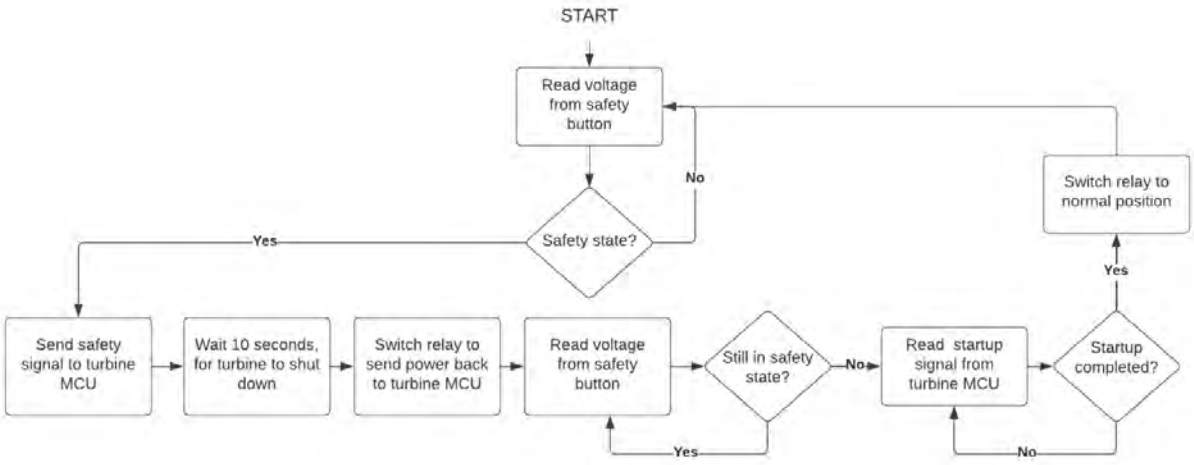

Figure 18: Finite state diagram for load MCU

2.5 Structural Design

In the Competition's first offshore-themed challenge, the objective of our turbine' structure was to support the turbine at both parked and operating conditions with wind speeds of up to 22 m/s at sea level. The goal of the offshore foundation was to secure the turbine in the simulation tank with minimal horizontal displacement–ideally less than 6 mm in accordance with competition rules–and with no sinking or tilting up to maximum operating conditions. Additional design goals were to minimize mass and facilitate installation.

Major loading conditions on structures parts include a thrust load of 28.33 N on the rotor in maximum wind speeds, a maximum rotor rotation speed of 1500 rpm, and the weight of the turbine of

34.3 N. Given that the center of the rotor is 84 cm above the sand level, the moment on the foundation due to the thrust load on the rotor will be the main mode of failure for the turbine. A complete list of safety factors can be found in Appendix D.

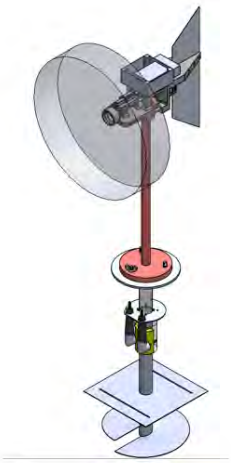

Figure 19. Full structural assembly mechanical drawing

2.5.1 Offshore foundation design, fabrication, and testing

As part of the design process, we researched current industry practices for offshore wind turbine (OWT) foundations. In industry, choosing the type of foundation depends on a number of factors including water depth, soil type, loading characteristics, and cost. The OWT foundation types that are currently used in industry are gravity beds, suction caissons, monopiles, and jacket foundations. The most frequently used foundation typology for OWTs are large-diameter, hollow monopiles, making up around 75% of all fixed-bottom OWT foundations.

Monopiles are well suited for shallow-water, fixed bottom OWT foundations because of their simplicity, low cost, and reliability. Thus, our team decided to begin the design process with a monopile and modify it throughout design iterations.

Given the limited bounding box for the foundation in the competition rules, a strict monopile would not have been effective as it could not go deep enough into the soil to provide adequate lateral support. So, a series of modifications were proposed, including the addition of a helical plate at the bottom of the pile, and a flat plate at the top. The helical plate would functionally convert the monopile into a screw pile, which makes installation more complicated, but provides the extra lateral support that was needed. The flat plate at the top also provides some lateral support, but serves mainly to prevent the foundation from sinking.

Figure 20. Foundation prototype

A suction caisson was also considered due to its lightness, simplicity, and ability to efficiently maximize the use of the foundation's bounding box. However, manufacture and testing of a foundation of this typology has not yet been conducted.

To manufacture the foundation, we selected all steel parts in accordance with the ferrous metal requirement. The 1.5 in outer diameter center tube is 14.96 in (38 cm) tall and made from low-carbon steel. The two plates were laser cut from 0.059 in (1.5 mm) mild steel. The top plate maximizes the allowed volume of the foundation in the sand, having been cut to 9.84 in by 9.84 in (25 cm by 25 cm) in area, and welded onto the center tube 5.90 in (15 cm) from the bottom of the foundation. The helical plate is 9.84 in (25 cm) in diameter, and forms one full revolution with a pitch of 1.5 in. The two plates were welded onto the center tube using mild steel MIG wire in accordance with the ferrous metal requirement. We also commissioned a stub prototype to be machined by our University's professional shop.

We tested our foundation's resistance to horizontal deflection and tilting in a tank similar in size to that at competition. The tank was 24 in long by 24 in wide by 18 in tall and filled with sand and water to depths given by competition regulations. After installation, 3.5 kg of weights were placed on top of the stub to simulate the weight of the turbine. Then, lateral load was applied by tying a cable to the top of the stub and hanging a bucket to be filled with sand over the side of the tank using a pulley. The foundation was loaded by incrementally adding sand of known mass to the bucket until (a) the foundation deflected 6 mm in the horizontal direction and subsequently (b) the foundation tilted substantially. The deflection was measured using a spring-loaded dial gauge.

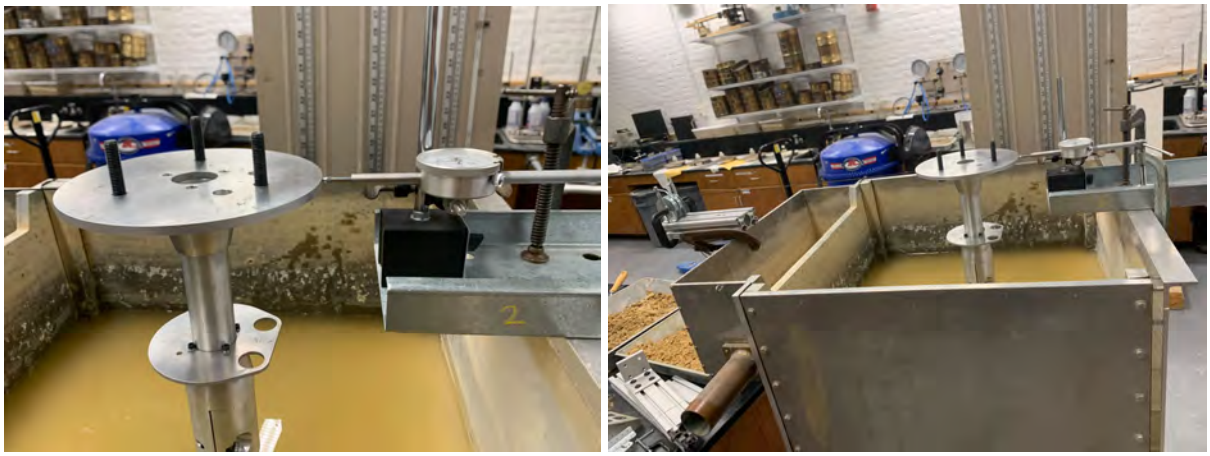

Figure 21. Offshore foundation testing set up

Since the foundation was loaded at the top of the stub, the equivalent load on the rotor had to be calculated, accounting for the longer moment arm. Unfortunately, we did not get desired results from our foundation design. In an attempt to improve the foundation's performance, we modified the design we had by adding removable walls, shown in Figure 22. However, the unmodified and modified design performed about the same. These results do not meet our goal of withstanding an estimated 28 N of thrust force on the rotor. Given more time, we would have liked to fabricate and test a caisson design as well.

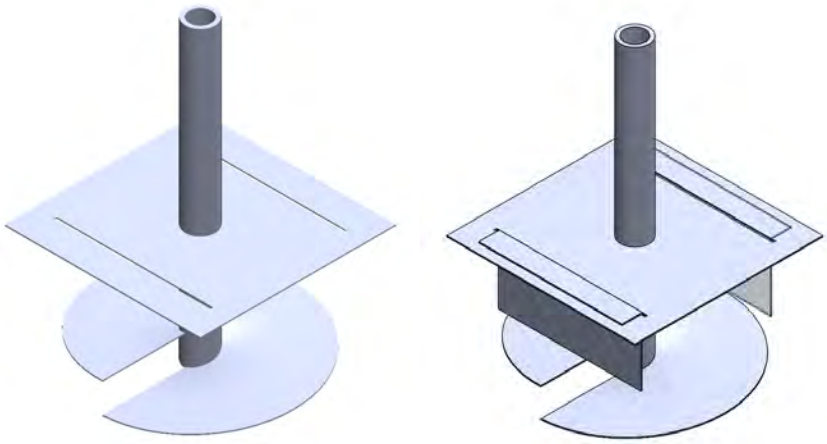

Figure 22. Foundation without "walls" (left) and with "walls" (right)

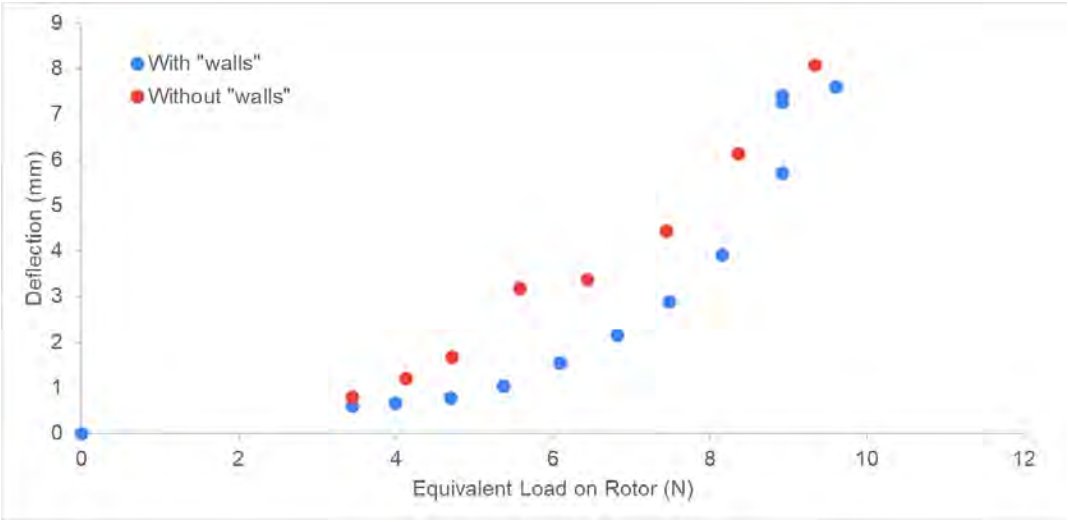

Figure 23. Deflection vs. Equivalent load on rotor

To install the foundation without touching the water, an installation tool was designed. The tool clamps onto the top of the foundation tube via two tightened bolts to provide greater torque for twisting the foundation into the sand. The tool is fabricated from 1.5 in inner diameter tubing and 6 in long "handles" welded onto the outer diameter. The tool is made from 6061 aluminum for weight reduction and ease of manufacturing. The tool's outer diameter is 14 in, from handle end-to-end, which will give adequate room to maneuver in the offshore simulation tank.

2.5.2 Nacelle

The nacelle was 3D printed from ABS. The objective of the design was to support the cantilevered rotor shaft and house all components in a compact space, reducing frontal area and protecting most of the electronic components from the water. The nacelle comprises two parts that clamp onto the yaw system's bearing housing using bolts for ease of subsystem assembly and disassembly. Bearings press-fitted into holes in the front nacelle part support the rotor shaft and reduce vibration.

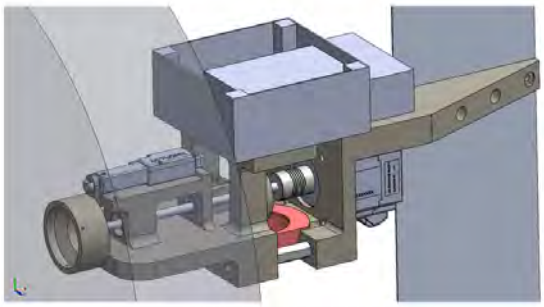

Figure 24. Nacelle mechanical drawing

2.5.3 Passive yaw system design

This year, there was less focus on the yaw system since the only competition requirement was yaw capability. The proven passive yaw system from last year's team was adapted for this year's turbine with the addition of a large tail fin to direct the rotor into the wind. The system is designed to minimize friction and withstand maximum loading conditions. The 3220JR Tapered Roller Bearing takes the majority of the axial load and the 60/22 deep groove ball bearing takes most of the bending moment from the thrust on the rotor. The housing for the two bearings is machined from 6061 aluminum.

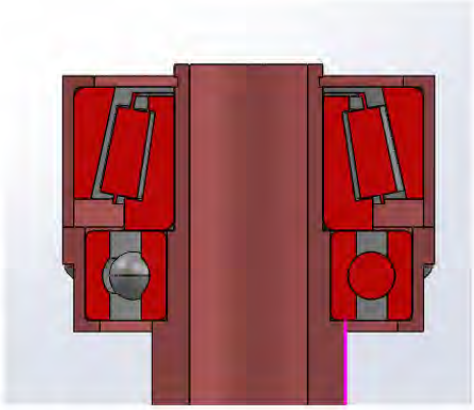

Figure 25. Passive yaw bearing system

2.5.4 Tower-base assembly

The tower-base assembly was also replicated from last year's proven design. Both the tower and base were machined from 6061 aluminum and brazed at the joint. Last year's design was validated to withstand more than 70 N·m of load in laboratory testing.

2.6 Final Assembly

After the independent development of all the subsystems, we proceeded to the final assembly of the turbine. The main component used to integrate all subsystems was the nacelle. We first mounted the nacelle on the tower and then connected the generator, 3-phase rectifier, and turbine electronics to the back of the nacelle. Then, we mounted the pitch system with the blades to the front of the turbine and connected the generator shaft to the rotor shaft using a shaft coupling. We also secured the linear actuator and connected it to the blade pitch system, while also adding the solenoid and the braking disc on the rotor shaft. Finally, we added the tail fin and placed the structure on the stub.

3.0 Commissioning Checklist

- ☐ Feed power and communication wires (that will connect the turbine and load) through the foundation
- ☐ Secure foundation into offshore simulation tank using installation tool and provided bubble level, ensuring ends of wires and all connectors stay out of water
- ☐ Feed the turbine-side end of the wires through the stub and mount the stub onto the foundation
- ☐ Assemble all mechanical components of the wind turbine outside of the wind tunnel
- ☐ Ensure all turbine electronics are in the enclosure and mount them on the nacelle of the turbine
- ☐ Attach electrical leads for the linear actuators (5V, signal, ground) and encoder to the turbine electronics
- ☐ Feed the turbine end of the wires through the tower and fix the tower onto the stub
- ☐ Attach all wires from tower to the corresponding connectors in the electronics enclosure
- ☐ Attach electrical lead from the turbine electronics ground to the turbine tower (which is electrically connected to the stub)
- ☐ Connect power lines to PCC (using the Anderson Powerpole connectors)
- ☐ Connect the safety button wires (using the JST connectors)
- ☐ Connect communication wires from the turbine to the load and ensure all load electronics are in the load enclosure
- ☐ Connect load MCU to wall power

4.0 Enumeration of Influence of Previous Design Reports

Our team this year decided not to do a counter-rotating design for the 2022 competition due to difficulties encountered last year with the transmission system and power production. Rather, the team decided to pivot to a single-rotor horizontal axis turbine and focus on making system-level improvements and exploring unique design concepts such as dimpled blades.

Although the transmission system was simplified to minimize power losses from more interfaces, we decided to use the same BL23E22-02 generator as last year's JHU team because it continued to outperform new motor considerations.

One of the main changes in the electronics and control systems compared to last year was the decision to use 2 MCUs, one on the turbine side and one on the load side. This decision reduced the complexity of last year's transistor-based system and helped decrease power consumption (since the load microcontroller is wall powered). This system also eliminated timing issues, since delays could now be

implemented more precisely in the code, without the need to resolve instability issues of digital components.

Another addition to this year's turbine is the complimentary mechanical braking system using a solenoid. In this year's design, the blade pitching brake relied entirely on the microcontroller being powered and functioning properly. Therefore, there would not be a safe way to shut down the turbine in the case of an electrical malfunction. For this reason, we decided to add a mechanical brake as a fail-safe mechanism that would be triggered upon interruption of power. This addition is useful for handling potential malfunctions and as a locking mechanism during normal braking after the rotor's speed reduction from blade pitching.

For the structural design, the nacelle design was different to support the addition of a tail fin and accommodate the lack of transmission system. We used proven designs from last year for the yaw, tower, and base designs. The offshore foundation was new this year.

For rotor and blade design, we used last year team's TSR and 2019 competition winner California Maritime University's blade geometry information for our initial blade geometry optimization in Qblade. We also used a rotor hub and active pitch control system from last year for our pitch control.

5.0 Appendix

5.1 Appendix A: Additional Mechanical Drawings of Nacelle

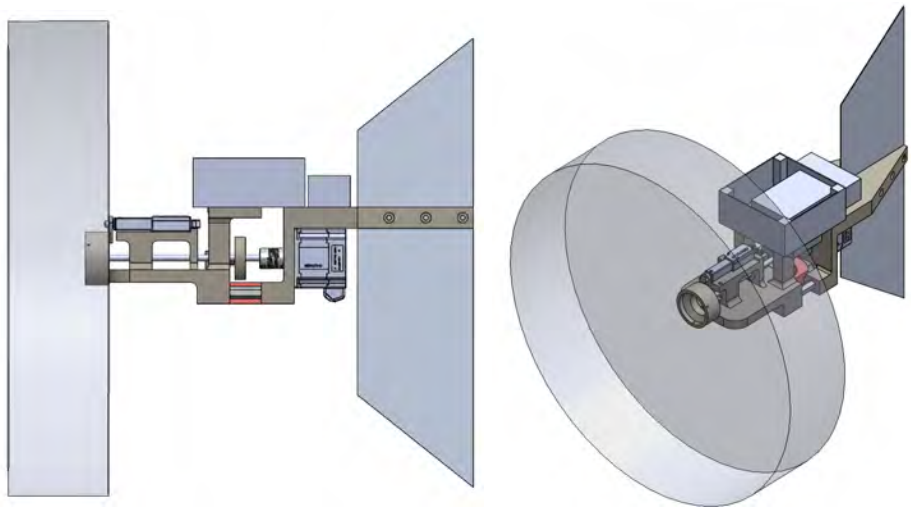

5.2 Appendix B: Foundation Testing

5.3 Appendix C: Variable Load

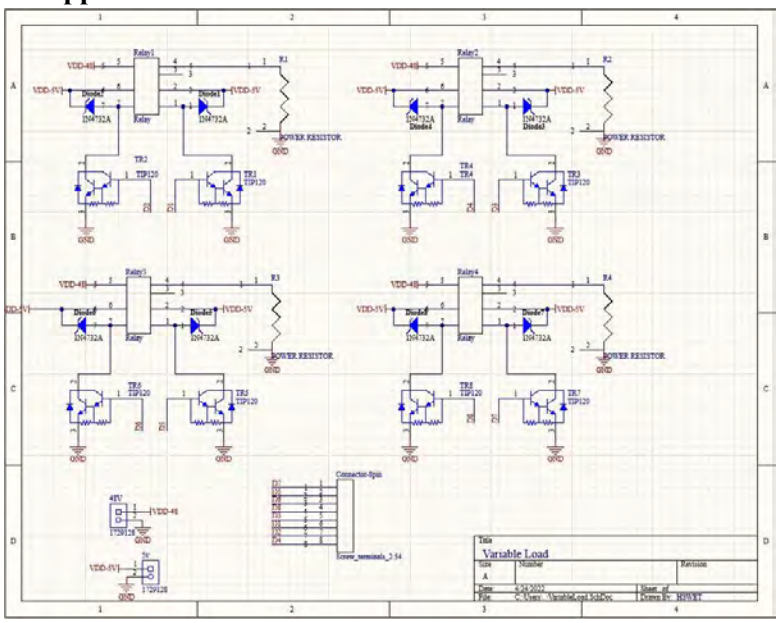

5.4 Appendix D: Safety Factors

Component	Safety Factor
Tower-base joint	5.72
Foundation in power testing	1.2
Foundation in durability testing	.42

6.0 References

[1] Raju Kumar, Priyanka Jhawar, Sanjay Kalraiya, "A CFD Analysis of a Wind Turbine Blade Design at Various Angle of Attack and Low Reynolds Number" International Journal of Scientific Research & Engineering Trends (2016), Volume 2, Issue 5

[2] Chen, S., 2020, "Numerical Investigation of Wind Turbine Airfoils under Clean and Dusty Air Conditions," Ph.D. thesis, Washington University in St. Louis, from https://openscholarship.wustl.edu/cgi/viewcontent.cgi?article=1577&context=eng_etds

[3] Singh, R.K., Ahmed, M. R., Zullah, M. A., and Lee, Y. H., 2012, "Design of a low Reynolds number airfoil for small horizontal axis wind turbines," Renewable Energy, Volume 42 66-76, from https://doi.org/10.1016/j.renene.2011.09.014

[4] airfoiltools NACA6409 http://airfoiltools.com/airfoil/details?airfoil=n6409-il

[5] Schmitz, G, "Theorie und Entwurf von Windrädern optimaler Leistung (Theory and design of windwheels with an optimum performance)", Wiss. Zeitschrift der Universität Rostock, 5. Jahrgang 1955/56

[6] Kim, Youjin & Al-Abadi, Ali & Delgado, Antonio. (2016). Strategic Blade Shape Optimization for Aerodynamic Performance Improvement of Wind Turbines. 10.1115/GT2016-56836

[7] Hiskey, Daven. "Why Golf Balls Have Dimples." November 28, 2012. https://www.todayifoundout.com/index.php/2010/12/why-golf-balls-have-dimples/.

[8] Johny, Robin K. "Design and Analysis of Dimple Arrangement on a Small Wind Turbine Blade." International Journal of Innovative Technology and Exploring Engineering 9, no. 2 (2019): 3552–57. https://doi.org/10.35940/ijitee.b6476.129219.

[9] Sedighi, H., Akbarzadeh, P., and Salavatipour, A., "Aerodynamic Performance Enhancement of Horizontal Axis Wind Turbines by Dimples on Blades: Numerical Investigation," Energy, 195 (2020), https://doi.org/10.1016/j.energy.2020.117056.

[10] Rajaram Narayanan, M., Nallusamy, S., Ragesh Sathiyan, M., "Design and Analysis of a Wind Turbine Blade with Dimples to Enhance the Efficiency through CFD with Ansys R16.0." MATEC Web of Conferences (2018), 207, https://doi.org/10.1051/matecconf/201820702004.

[11] J. Keith. Capacitor Input Filter Calculation [Online]. Available: https://www.electroschematics.com/capacitor-input-filter-calculation/

[12] P. Evans. (2019, May. 30) Three Phase Voltage + Calculations [Online]. Available: https://theengineeringmindset.com/three-phase-voltage-calculations/